Journal of Photochemistry & Photobiology, A: Chemistry 443 (2023) 114812

Contents lists available at ScienceDirect

Journal of Photochemistry & Photobiology, A: Chemistry

journal homepage: www.elsevier.com/locate/jphotochem

Bismuth oxychloride microcrystals decorated carbon foams based on waste polyurethane elastomer for enhanced removal of methylene blue

Mahitha Udayakumar [a,b], Nikita Sharma [a], Klara Hernadi [c], Matjaž Finšgar [d], Blaz Likozar [e], Kocserha István [f], Máté Leskó [c], Dániel Attila Karajz [g], Imre Miklós Szilágyi [g], Zoltán Németh [a,*]

[a] Advanced Materials and Intelligent Technologies Higher Education and Industrial Cooperation Centre, University of Miskolc, 3515 Miskolc, Hungary
[b] Institute of Chemistry, University of Miskolc, 3515 Miskolc, Hungary
[c] Institute of Physical Metallurgy, Metal Forming and Nanotechnology, University of Miskolc, 3515 Miskolc, Hungary
[d] Faculty of Chemistry and Chemical Engineering, University of Maribor, Smetanova ulica 17, SI-2000 Maribor, Slovenia
[e] Department of Catalysis and Chemical Reaction Engineering, National Institute of Chemistry, Hajdrihova 19, 1001 Ljubljana, Slovenia
[f] Institute of Ceramic and Polymer Engineering, University of Miskolc, 3515 Miskolc, Hungary
[g] Department of Inorganic and Analytical Chemistry, Faculty of Chemical Technology and Biotechnology, Budapest University of Technology and Economics, Muegyetem Rakpart 3, 1111 Budapest, Hungary

ARTICLE INFO

Keywords:
Carbon foam
Bismuth oxychloride
Nanocomposite
Methylene blue
Photocatalytic activity

ABSTRACT

Multicomponent materials containing nanoscale structures, the so-called "nanocomposites" are one of the fastest-growing areas of photocatalytic research. In this study, the nanocomposites of bismuth oxychloride (BiOCl) with porous carbon foam (CF) derived from waste polyurethane (PU) elastomers were developed by a simple hydrothermal method, and the photocatalytic performance of the as-prepared materials was investigated. The structure, morphology and optical properties of the composites were characterized in detail. The photocatalytic activity of the samples was evaluated by studying the degradation of methylene blue (MB) under UV-A irradiation. Even at a high MB concentration (0.5 mmol/L), excellent photocatalytic activity was observed, with an overall removal efficiency of 99.0% in 100 min of irradiation. Kinetic studies were also carried out for the degradation of MB by pristine BiOCl and CF-BiOCl. The photodegradation rate constants were evaluated by fitting the kinetic data with a pseudo-first-order model, and the rate constants of CF-BiOCl composites were higher than that of pristine BiOCl. The enhanced activity of the composites was due to the well-connected heterojunction interface, improved hydrophilicity, more reactive sites, and effective separation of photogenerated charges. Thus, our work combines the valuable waste PU-derived CFs with BiOCl, which provides a strategy to achieve circular economy and environmental remediation objectives.

1. Introduction

Semiconductor photocatalysis is a potential green technology for environmental and energy issues [1]. A series of semiconductor photocatalysts, including metal oxides, oxynitrides, sulfides, and halides, are widely employed in the photoreduction of CO_2, water splitting and photodegradation of pollutants [2–4]. In recent times, researchers have focused on novel photocatalytic materials to overcome the low photoconversion efficiency of catalysts [5]. Bismuth oxyhalides (BiOX, X = Cl, Br, I) are a relatively new class of semiconductor photocatalysts that have the advantages of visible light response, good chemical stability, non-toxicity, appropriate band gap, and controllable morphology [6,7]. Among them, BiOCl is one of the promising candidates due to its good crystalline structure, high stability, low cost, and low toxicity [8]. BiOCl has a tetragonal structure of the P4/nmm space group, which consists of [Cl-Bi-O-Bi-Cl] quinary layers stacked together by the non-bonding interaction through the Cl atoms along the c-axis [9]. It has a wide bandgap (~3.2–3.5 eV), which makes it UV-active and is being applied in areas of UV light detection, solar water splitting, and photocatalytic wastewater purification. BiOCl has been prepared in well-defined nanostructures that influence its overall photocatalytic performance. Different morphologies of BiOCl have been reported, for example, BiOCl

* Corresponding author.
E-mail addresses: kemudaya@uni-miskolc.hu (M. Udayakumar), nikita.sharma@uni-miskolc.hu (N. Sharma), femhernadi@uni-miskolc.hu (K. Hernadi), matjaz.finsgar@um.si (M. Finšgar), Blaz.Likozar@ki.si (B. Likozar), istvan.kocserha@uni-miskolc.hu (K. István), askmate@uni-miskolc.hu (M. Leskó), karda412@gmail.com (D.A. Karajz), szilagyi.imre.miklos@vbk.bme.hu (I.M. Szilágyi), kemnemet@uni-miskolc.hu (Z. Németh).

https://doi.org/10.1016/j.jphotochem.2023.114812
Received 6 February 2023; Received in revised form 14 April 2023; Accepted 29 April 2023
Available online 3 May 2023

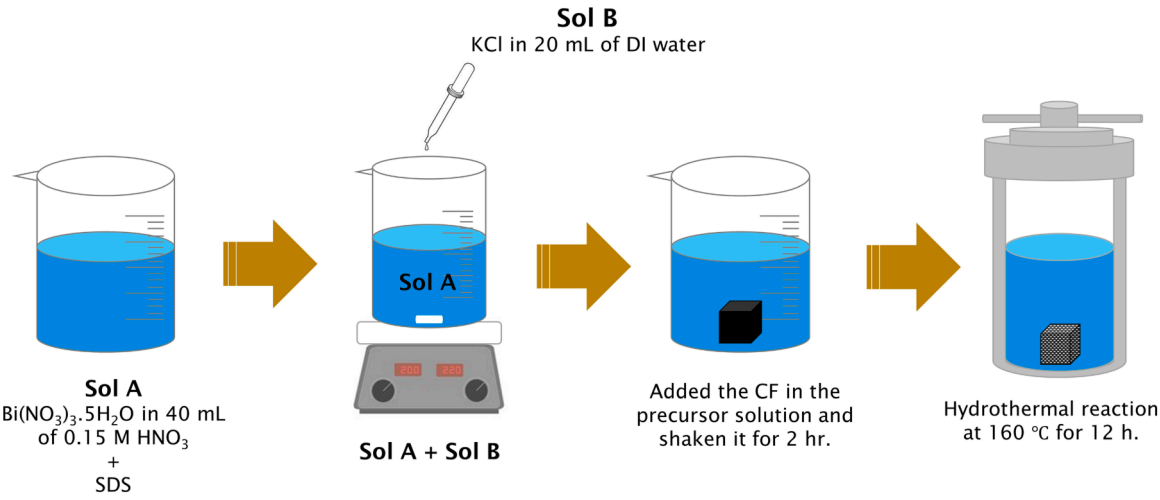

Fig. 1. A flow diagram for the synthesis of CF-supported BiOCl.

nanosheets [10], hollow BiOCl microspheres [11], BiOCl nanocubes [12], etc.

However, based on its physical properties such as poor charge mobility and fast charge recombination, BiOCl has limitations in photocatalytic reactions [13]. To overcome these limitations, the light response of the BiOCl photocatalyst has been extended by various techniques such as morphology control [14], crystal facet exposure [15], self-doping [16], heterojunction construction [17], surface modification [18], and supports [19]. Among them, the construction of heterojunction is a simple and efficient approach [20]. Xie et al. [21] used BiOCl and $Bi_2O_2CO_3$ to form heterojunction, significantly improving photocatalytic performance under ultraviolet and visible light. Likewise, Bi_2WO_6-BiOCl heterojunction with enhanced photocatalytic activity for efficient degradation of oxytetracycline was reported by Guo et al. [22]. Besides, the operational problems associated with recovering and reusing BiOCl powder catalysts prevent its large-scale implementation. The use of support is intended to overcome this limitation. The use of carbon supports contributes to (i) faster sedimentation and easier recovery of the photocatalyst from the reaction medium, (ii) the high specific surface area provides more reactive sites for the reaction, and (iii) the heterojunction formed with the semiconductors prevent the recombination of e^--h^+ pairs. Combining BiOCl with functional porous carbon improves photocatalytic activity due to their high adsorption capacity, good electron transfer ability and chemical stability [23]. Generally, the BiOCl powder has low adsorption capacity owing to its less specific surface area (S_{BET} – typically 5–10 m^2/g) or active sites. The composite of BiOCl with carbon materials such as activated carbon [19,24], biochar [25], carbon nanotubes (CNTs) [26,27], carbon fibers [28] and graphene [29] exhibited enhanced adsorption due to improved surface area and good photocatalytic response. However, these carbons still suffer from some drawbacks, e.g., high production costs, handling of powdered materials and complicated acid purification steps. On the contrary, the 3D hierarchical porous carbon material derived from the waste would be economical and the best choice to overcome these shortcomings. One such material is carbon foam (CF), which is an excellent support material for nanomaterial catalysts, owing to its hierarchical porous structure, high S_{BET}, low cost, non-toxicity and high stability [30].

Dye pollution has become one of the major contributors to water pollution across the world. More than 100,000 dye products have been discharged into the aquatic environment, which is toxic and carcinogenic [31]. The dyes released into the water bodies are hard to be degraded under natural conditions. One of the highest-consuming dyes in the industries is methylene blue (MB), for colouring silk, wool, cotton, and paper [32]. The removal of methylene blue from industrial wastewater has been investigated using various methods such as the chemical precipitation method, enzymatic process, electrochemical removal, membrane filtration, and physical adsorption methods [33]. Each method has its advantages and limitations. Adsorption is the simplest method for the effective removal of MB by utilizing low-cost and abundant adsorbents e.g., carbon-based adsorbents. In our recent work, we reported the synthesis of activated CFs using waste polyurethane elastomer templates and evaluated their methylene blue (MB) adsorption capacity as high as 592 mg/g [34].

Though the adsorption removes the dyes from the wastewater, it does not necessarily degrade the pollutants into eco-friendly products. Hence, the integration of adsorption and an advanced oxidative process such as photocatalysis can enhance the overall removal efficiency. Some earlier works have reported the applicability of CFs as support for the semiconductor catalyst and showed good photocatalytic performance and overall pollutant removal rate. For instance, a CF-loaded nano-TiO_2 photocatalyst was synthesized and the degradation of methyl orange evaluated its photocatalytic activity as a model pollutant [35]. The work of Qian et al. [36] reported the preparation of mesoporous TiO_2 films coated on CF based on polyurethane foam for enhanced photocatalytic oxidation of VOCs. Moreover, a flower-like BiOBr/CF composite with enhanced visible-light-driven catalytic activity was synthesized using the double-template bionic mineralization method with CF as a hard template and polyvinylpyrrolidone (PVP) as a soft template for the removal of Rhodamine B [37]. There are some works which reported the BiOCl-assisted photodegradation of dye [38–41]. To the best of our knowledge, there has been no study on the preparation of CF-supported BiOCl composites as photocatalysts. Therefore, the preparation and photocatalytic performance of the CF-BiOCl composite contribute to a new research direction.

In this work, the CF with high S_{BET} (2172 m^2/g) [34] produced from waste polyurethane elastomer template was used to synthesize CF-BiOCl composite in which the BiOCl micro flowers and plates were immobilized on the CF surface. Moreover, it was reported that the use of a shape-controlling agent like PVP improved the properties of the composite by regulating the crystal structure of BiOBr on CFs [37]. As a widely and efficiently used anionic surfactant, sodium dodecyl sulfate (SDS) has been used for the synthesis of novel morphologies of nanostructures [42]. Hence, herein the role of SDS in the formation of BiOCl nanostructure on the CFs was also investigated. Further, the photocatalytic performance of the composites was evaluated by the degradation of methylene blue (MB) as a model pollutant under UV light irradiation. The usage of waste PU elastomer-derived CF as a support material for BiOCl and its applicability in photocatalytic degradation of MB dye was studied in line with multiple Sustainable Development

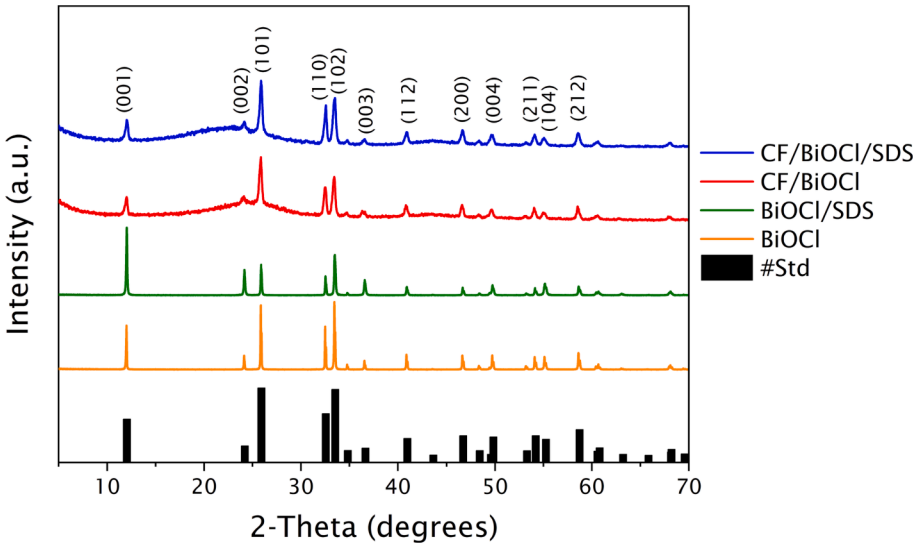

Fig. 2. XRD diffractogram of pristine BiOCl and CF-BiOCl composites with and without surfactant.

Table 1
Results of XRD and nitrogen sorption test.

Samples	XRD analysis		Nitrogen sorption test		
	Mean primary crystallite size (nm)	(001), (101) and (102) intensities ratio	S_{BET} (m^2/g)	Total pore volume (cm^3/g)	Average pore diameter (nm)
BiOCl	83.2	0.68:1.00:1.05	4.9	0.009	7.1
BiOCl/SDS	61.1	2.21:1.00:1.32	2.8	0.009	12.7
CF/BiOCl	28.6	0.39:1.00:0.93	258.5	0.18	2.0
CF/BiOCl/SDS	28.5	0.39:1.00:0.91	34.8	0.026	4.8
JCPDS No. 4509949	N/A	0.54:1.00:0.98	N/A	N/A	N/A

Goals of the United Nations, e.g., Goals 6 (Clean water and sanitation) and 12 (Responsible consumption and production).

2. Materials and methods

2.1. Materials

Bismuth nitrate pentahydrate ($Bi(NO_3)_3{\cdot}5H_2O$), potassium chloride (KCl), SDS and nitric acid (HNO_3) (65%) were purchased from VWR International Ltd., Hungary. All the reagents were of analytical grade and used without further purification. As reported in our earlier work, the CFs prepared from the waste polyurethane elastomers were used as a support material [34]. MB dye (VWR International Ltd., Hungary) was used as a model pollutant in photocatalytic tests. Ultrapure water (resistivity of 18.2 MΩ cm) was used throughout the experiment.

2.2. Preparation of CF-BiOCl composites

A schematic representation of the synthesis procedure is given in Fig. 1.

Two types of composites were prepared with and without the addition of surfactant SDS. Firstly, 2 mmol of $Bi(NO_3)_3{\cdot}5H_2O$ was dissolved in 40 mL of 0.15 M nitric acid solution, denoted as 'Sol A'. 2 mmol of KCl was dissolved in 20 mL of deionized water, denoted as 'Sol B'. Then, SDS (0.4 g) was added to Sol A and stirred for 30 min to obtain a suspension. Subsequently, Sol B was added dropwise into the suspension and stirred for 30 min. Then, the CF (0.25 g) was added to the above mixture and shaken for 2 h. The mixture was transferred to a Teflon-lined® autoclave and allowed to react at 160 ℃ for 12 h. After self-cooling to room temperature, the solid product was washed with deionized water and ethanol several times. Finally, the composite was obtained by drying at 70 ℃ overnight. The as-prepared composite is named 'CF/BiOCl/SDS' and the composite without the addition of SDS is denoted as 'CF/BiOCl'. The same procedure was followed for the synthesis of pristine BiOCl except for the addition of CFs named 'BiOCl/SDS' (with SDS) and 'BiOCl' (w/o SDS).

The pristine BiOCl and the CF-BiOCl composites were also synthesized by doubling the precursors' concentration (4 mmol of ($Bi(NO_3)_3{\cdot}5H_2O$ and KCl) and surfactant (0.8 g of SDS) and their characteristics and photocatalytic performances are given in supplementary material.

2.3. Characterization

The crystal structure of the samples was characterized by X-ray diffraction (XRD) using a Rigaku Miniflex II diffractometer with a Cu K_α radiation source (30 kV and 15 mA) in a range of $3^\circ \leq 2\theta \leq 90^\circ$ with a scan speed of 0.01° 2θ/sec. The primary crystallite size (D) was calculated using the Scherrer equation given below:

$$D = \frac{K\lambda}{\beta cos\theta} \quad (1)$$

where K is a dimensionless shape factor, λ is the wavelength of the X-ray, β is full-width at half maximum (FWHM) of the diffraction peaks, and θ is the Bragg angle [43].

Nitrogen adsorption–desorption experiments were carried out at 77 K to determine the Brunauer-Emmett-Teller [44] (BET) specific surface area using an ASAP 2020 instrument (Micromeritics Instrument Corp., Norcross, GA, USA). Before each measurement, the samples were degassed by holding them at 90 °C for 24 h.

Raman spectroscopy measurements were carried out using a high-resolution Raman spectrometer (Nicolet Almega XR, Thermo Electron

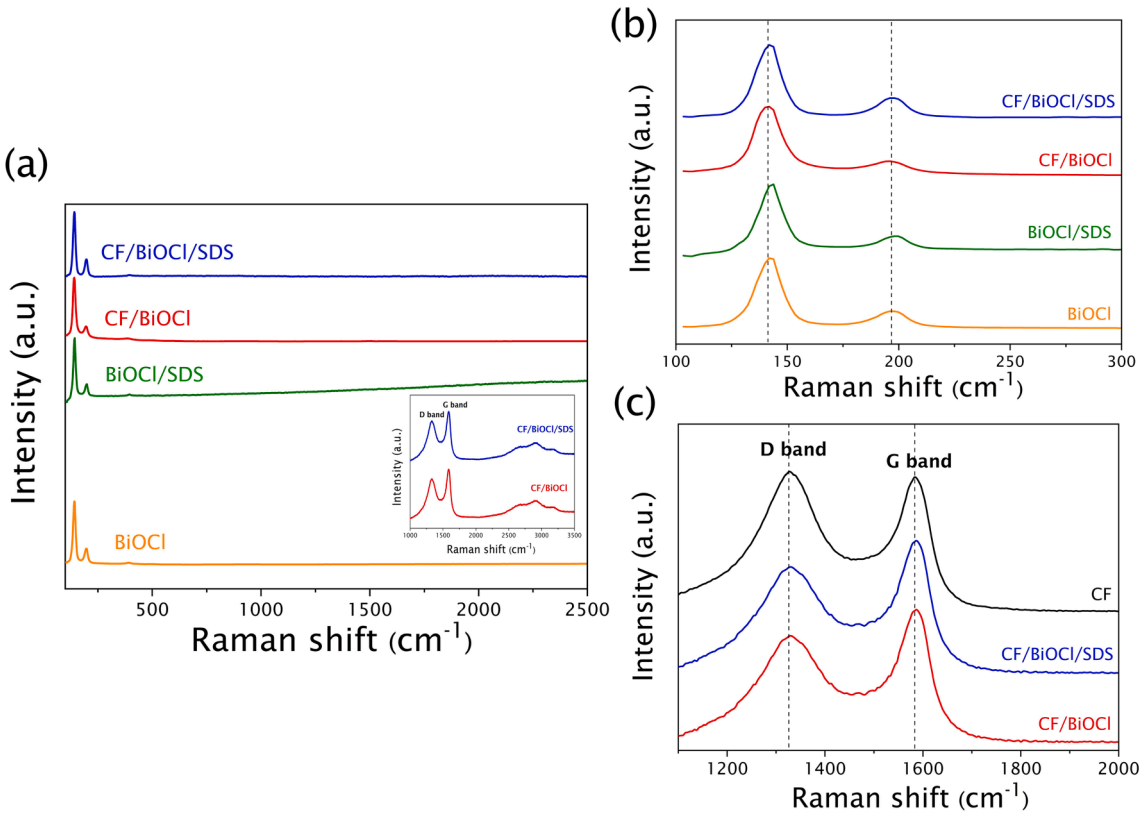

Fig. 3. Raman spectra of BiOCl and composites and the inset in (a) showing the D and G bands of CF in CF-supported BiOCl, (b & c) the spectra of (a) were zoomed in for visibility.

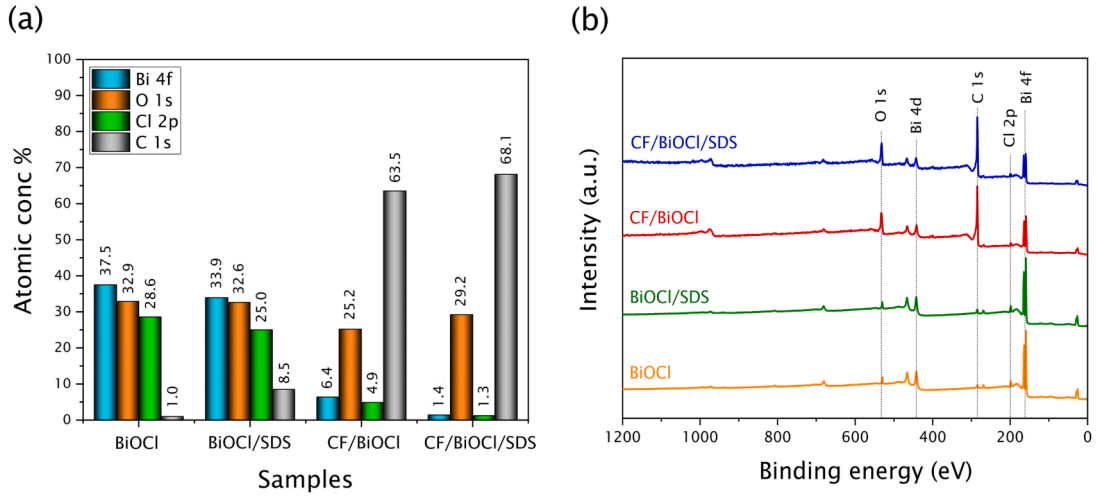

Fig. 4. (a) Elemental composition, and (b) XPS survey spectra of pristine and CF-supported BiOCl samples.

Corporation, Waltham, MA, USA) equipped with a 532 nm Nd: YAG laser (50 mW).

The composition and chemical states of the samples were investigated by X-ray photoelectron spectroscopy (XPS) using the Supra plus instrument (Kratos, Manchester, UK) controlled by ESCApe 1.4 software (Kratos). The instrument was equipped with an Al K_α excitation source. The binding energy scale was corrected using the C-C/C-H peak at 284.8 eV in the C 1s spectra. During the XPS analysis, the charge neutralizer was on. The spectra were acquired at a 90° take-off angle on a 300 by 700-μm spot size. Survey spectra and high-resolution spectra were measured at pass energy of 160 eV and 20 eV, respectively. Background subtraction was performed using the Shirley background subtraction [45].

Scanning electron microscopy (SEM) was performed with Thermo Helios G4 PFIB Cxe to investigate surface morphology. The device was equipped with energy-dispersive X-ray spectroscopy (EDS) enabling the mapping of the samples. EDS maps and spectra were acquired using an acceleration voltage of 25 keV with a beam current of 13nA and a dwell time of 500 μs. For SEM analysis, the samples were deposited on sticky carbon tape.

Avantes AvaSpec-2048 spectrometer was used for measuring the diffuse reflectance spectra of the samples. The indirect band-gap energy was calculated using the Kubelka-Munk equation given as follows:

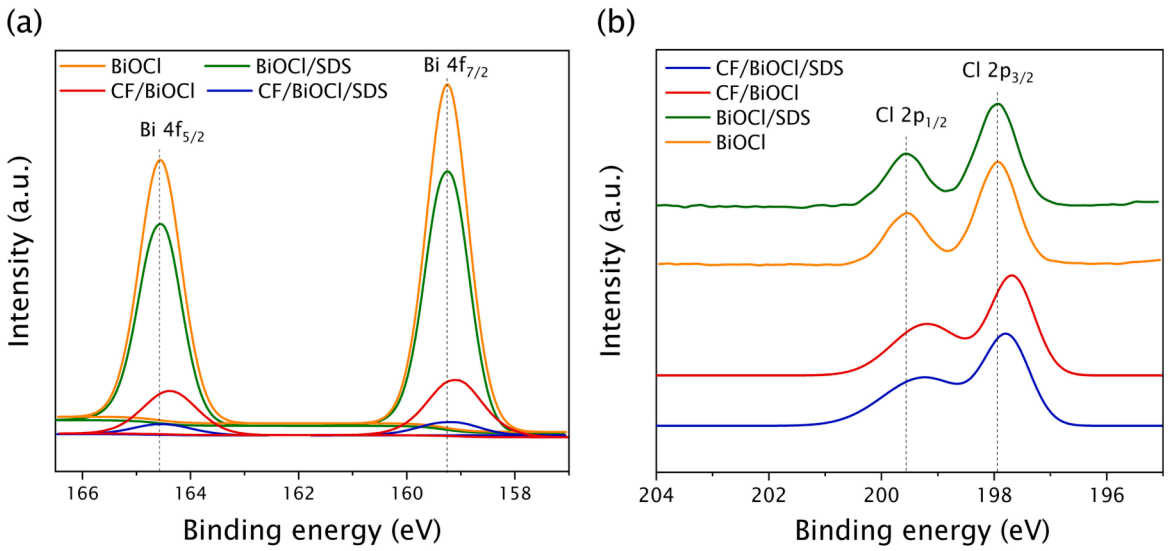

Fig. 5. XPS deconvoluted peaks of (a) Bi 4f, and (b) Cl 2p of pristine BiOCl and CF-BiOCl composites.

$$(F(R)h\nu)^{\gamma} = A(h\nu - E_g) \quad (2)$$

where h is the Planck constant, ν is the frequency of the incident photon, γ represents the nature of the electronic transition ($\gamma = 2$ for direct allowed transition and $\gamma = 1/2$ for indirect allowed transition), A is the proportionality constant, E_g is the band gap energy. Tauc plot ($(F(R)h\nu)^{1/2}$ *vs* photon energy ($h\nu$)) is used to determine the band gap of the samples. The electron transitions were evaluated by plotting the first derivative spectra $dR/d\lambda$.

2.4. Photocatalytic test

The photocatalytic activity of the composites was evaluated *via* the photodegradation of MB in an aqueous solution under ultraviolet irradiation using UV-A lamps for 120 min (300–500 W) with emission maxima of 315 and 375 nm. The initial concentrations of MB were taken as 0.05 mmol/L and 0.5 mmol/L. In each case, the catalyst of 200 mg was dispersed in 200 mL of MB solution and stirred in the dark for 2 h. The total irradiation time was 2 h under UV–A. Approximately 3.5 mL of the reaction suspension was removed in regular time intervals and filtered through a 0.22 μm syringe filter. The concentration of MB was measured using a UV–Vis light spectrophotometer (UV-M51) at an absorbance of 664 nm. The degradation and residual rates of MB were calculated using Eqs. (3) and (4):

$$\text{The degradation rate of MB} = \frac{c_0 - c}{c_0} \times 100\% \quad (3)$$

$$\text{Residual rate of MB} = \frac{c}{c_0} \times 100\% \quad (4)$$

where c_0 and c are the initial and final concentrations of MB, respectively.

The kinetics of the photocatalytic degradation rate of MB was determined using the Langmuir-Hinshelwood kinetic model, as given in Eq. (5):

$$\ln\frac{c_0}{c} = kt \quad (5)$$

The pseudo-first-order rate constant (k) was calculated from the slope of $\ln(c_0/c)$ *versus* irradiation time t.

3. Results and discussion

For a better understanding of the correlation between structure and function, the physicochemical properties of the blank and CF-supported BiOCl were widely studied and the results of samples prepared from 2 mmol of precursors are discussed in the following sub-sections.

3.1. Structural and surface properties

The crystal structure and the phase composition of pristine BiOCl and CF-BiOCl composites were investigated by XRD and the respective diffractograms are shown in Fig. 2.

All the diffraction patterns correspond well with tetragonal bismuth oxychloride (JCPDS No. 4509949). The XRD pattern of the pristine BiOCl shows intense diffraction peaks at 2θ values of 12.0°, 25.9°, and 33.5 ° corresponding to the crystal planes of (0 0 1), (1 0 1) and (1 0 2) respectively. On the other hand, the composites exhibit the major peaks at 2θ of 25.9° 32.6°, and 33.5° relative to the respective planes of (1 0 1), (1 1 0) and (1 0 2). No additional peaks from other impurities indicate the successful synthesis of BiOCl. The presence of amorphous background is evident through the peak widening (Fig. 2) due to the amorphous CF template. Compared to the pristine BiOCl, there is no significant change in the position of the diffraction peaks of the CF-BiOCl composite which means that the addition of CF does not alter the crystal structure of BiOCl. However, we could observe a little variation in the relative intensities of the peaks that points toward some changes in the crystal orientations. For instance, the dominant crystallographic orientation of pristine BiOCl (shown in yellow colour) is the (1 0 2) plane, but the addition of SDS enhanced the crystal growth along the (0 0 1) plane (shown in green colour), whereas, at higher precursors' concentrations (4 mmol), the predominant crystallographic orientation of pristine BiOCl with SDS is the (1 0 2) as shown in Fig. S1. On the other hand, the CF template regulated the growth direction of the BiOCl crystal in the (1 0 1) irrespective of the surfactant (shown by red and blue diffractograms).

The range of primary crystallite size calculated from the Scherrer equation (Eq. (1)), intensities ratio (calculated after the baseline corrections), S_{BET}, total pore volume and average pore diameter measured using nitrogen sorption test of the pristine BiOCl and the composites are given in Table 1. The pristine BiOCl showed a larger crystallite size of 83.2 nm, whereas the addition of SDS slightly reduced the crystallite size to 61.1 nm. On the other hand, relatively smaller crystallite sizes (~29 nm) were observed for both types of composites. Hence, the CF template supported the formation of smaller crystallites of the BiOCl, and the surfactant had no significant role in regulating the crystallite sizes in the case of composites.

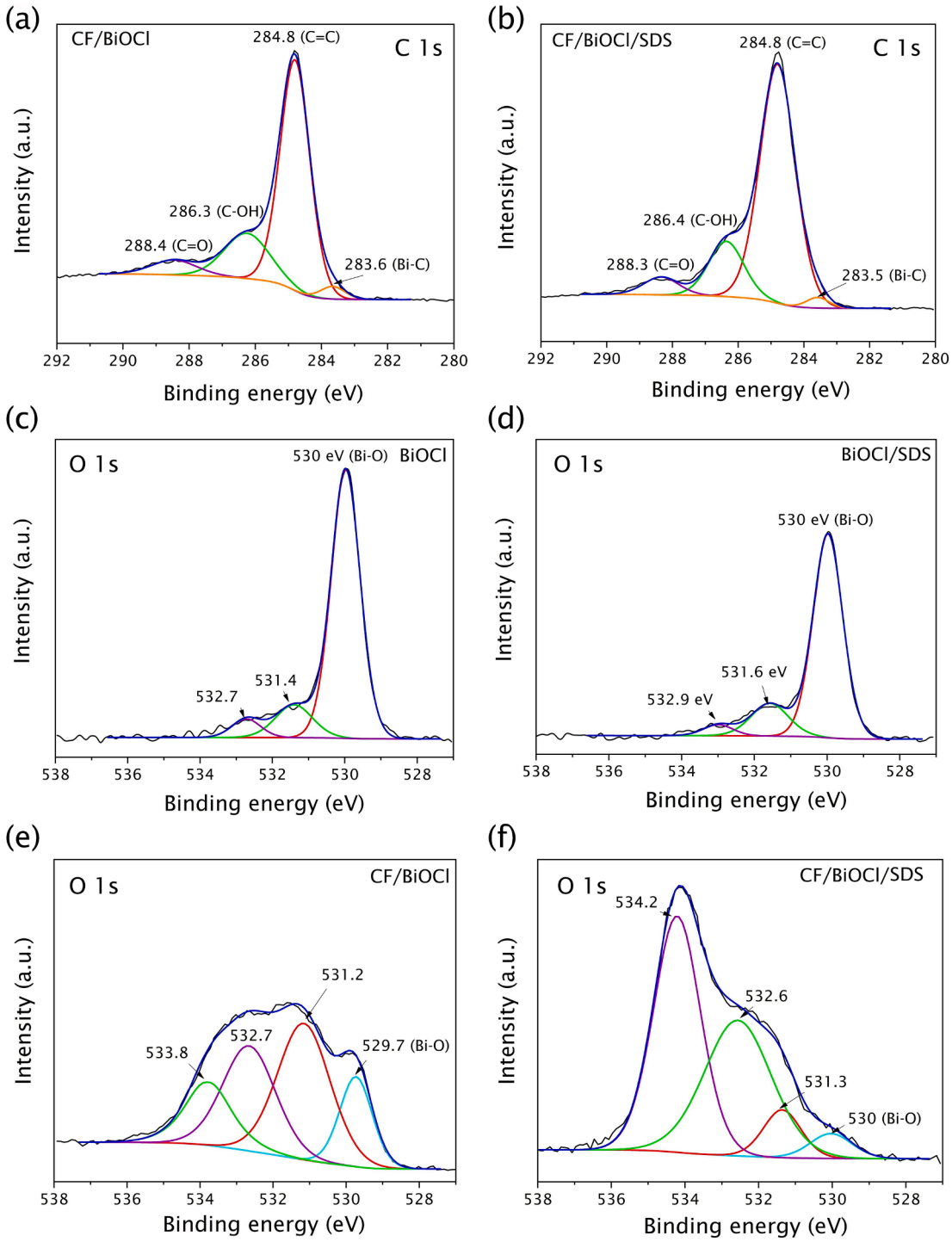

Fig. 6. XPS deconvoluted peaks of (a, b) C 1s, and (c-f) O 1s of pristine BiOCl and CF-BiOCl composites.

The S_{BET} of the blank samples was 2.8 m^2/g (BiOCl/SDS) and 4.9 m^2/g (BiOCl) which is true since the hydrothermal treatment leads to the formation of larger crystals. The S_{BET} of the pure CF was 2172 m^2/g [34], but after the formation of BiOCl crystals, the specific surface area drastically reduced for CF/BiOCl (258.5 m^2/g, which can be seen in Table 1), on account of the eventual blockage of the BiOCl nanoparticles in the pores of the CF. The reduction in the surface areas indicates that BiOCl has effectively grown on the surface of CF with sufficient interfacial interaction [23]. However, it got further reduced while using surfactant due to its excessive quantity, which could limit the diffusion of N_2 during measurement, thereby showing reduced surface area. As can be seen from Table 1, the CFs benefit the surface property of the composites with improved surface area (compared to blank BiOCl), which means a higher number of active sites which could enhance the photocatalytic activity of BiOCl and overall pollutant removal efficiency.

Raman spectra were used to evaluate the chemical structure of the composites. As shown in Fig. 3a, the peaks at 142, 198 and 392 cm^{-1} were present in the pristine BiOCl samples. The strong peak around 142 cm^{-1} corresponds to A_{1g} internal Bi-Cl stretching mode and another peak at 198 cm^{-1} belongs to E_g internal stretching mode of Bi-Cl. A very weak peak around 392 cm^{-1} belongs to E_g and B_{1g} bands due to the

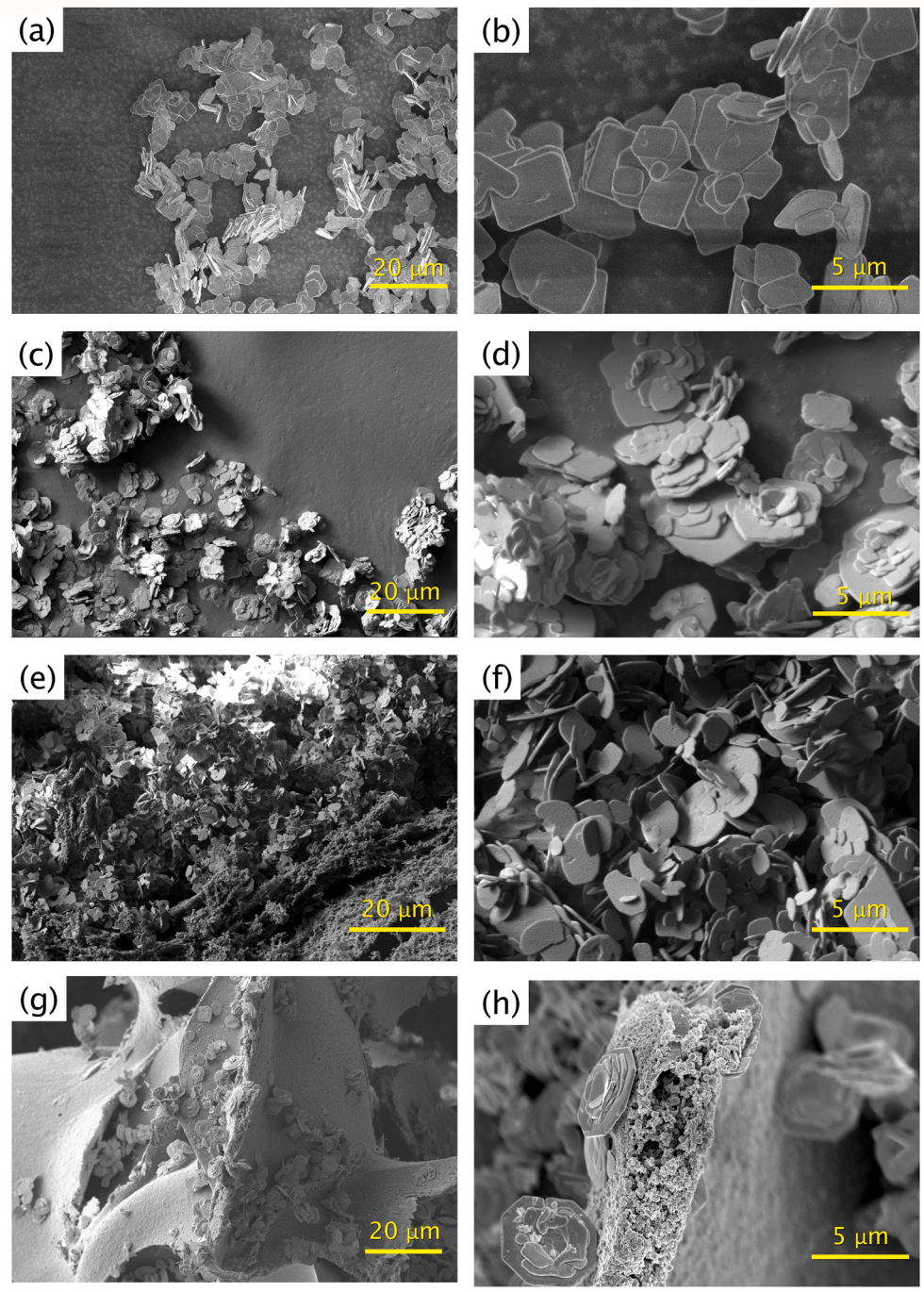

Fig. 7. SEM micrographs of (a, b) BiOCl, (c, d) BiOCl/SDS, (e, f) CF/BiOCl, and (g, h) CF/BiOCl/SDS.

motion of oxygen atoms. These spectra are in line with other earlier reports [24,46].

In the case of composites, the two noticeable peaks were slightly moved towards 141 cm^{-1} and 196 cm^{-1}, respectively, as shown in Fig. 3b. Moreover, the CF exhibited two characteristic peaks 1325 cm^{-1} and 1582 cm^{-1} (Fig. 3c), which belonged to the D and G bands. The D and G bands reflect the structural defects and the crystallinity of CFs, respectively. However, in the CF-supported BiOCl, the D and G bands moved towards 1329 cm^{-1} and 1588 cm^{-1}. These shifts represent the successful formation of composites and chemical interaction between CF and BiOCl.

To determine the composition and the interactions between CF and BiOCl crystals further, the surface chemical states of the samples were investigated using XPS. The surface atomic concentrations and the survey spectra of the samples are shown in Fig. 4a and b, respectively. Bi-, O-, Cl-, and C-containing species were present in all samples tested (Fig. 4b). The blank samples contain a higher atomic surface concentration of Bi, O, and Cl than the composites (Fig. 4a). The C-containing species in the blank BiOCl sample originated from the adventitious carbonaceous species and/or surfactant and/or impurities during synthesis. In the case of composites, the sample without surfactant (CF/BiOCl) showed a higher atomic surface concentration of Bi (6.4 at. %) and Cl (4.9 at. %) than CF/BiOCl/SDS (1.4 at. % of Bi and 1.3 at. % of Cl).

The high-resolution XPS spectra for Bi 4f and Cl 2p are shown in Fig. 5a and b. Bi 4f is composed of two peaks centred at 164.5 eV and

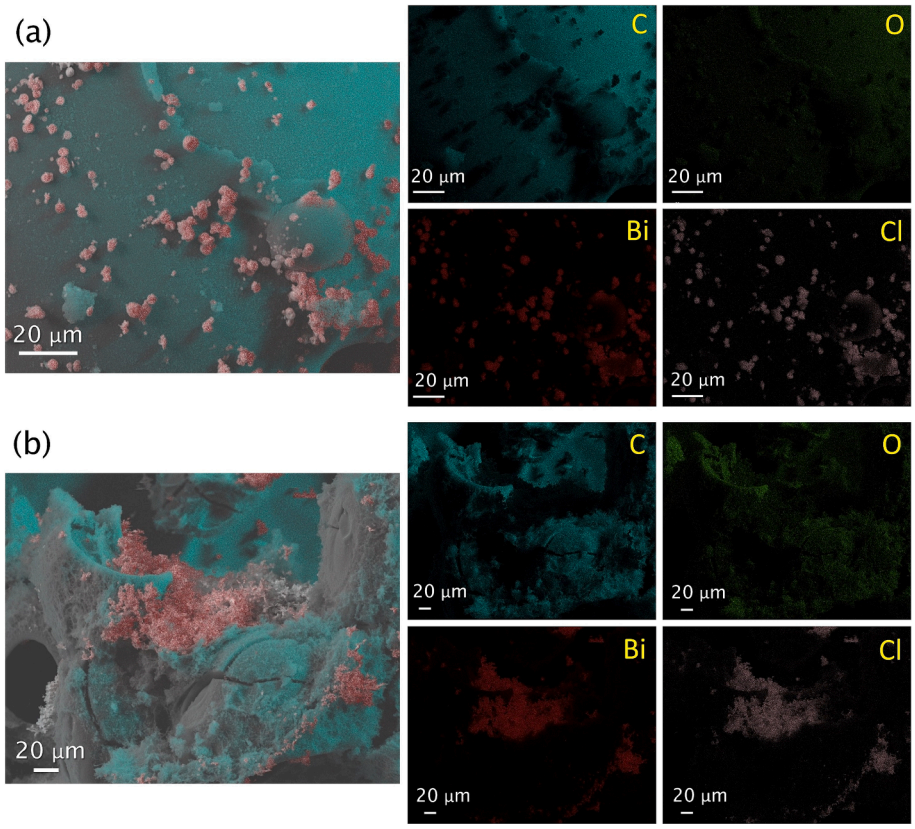

Fig. 8. EDX elemental mapping of Bi, O, Cl and C of (a) CF/BiOCl/SDS, and (b) CF/BiOCl.

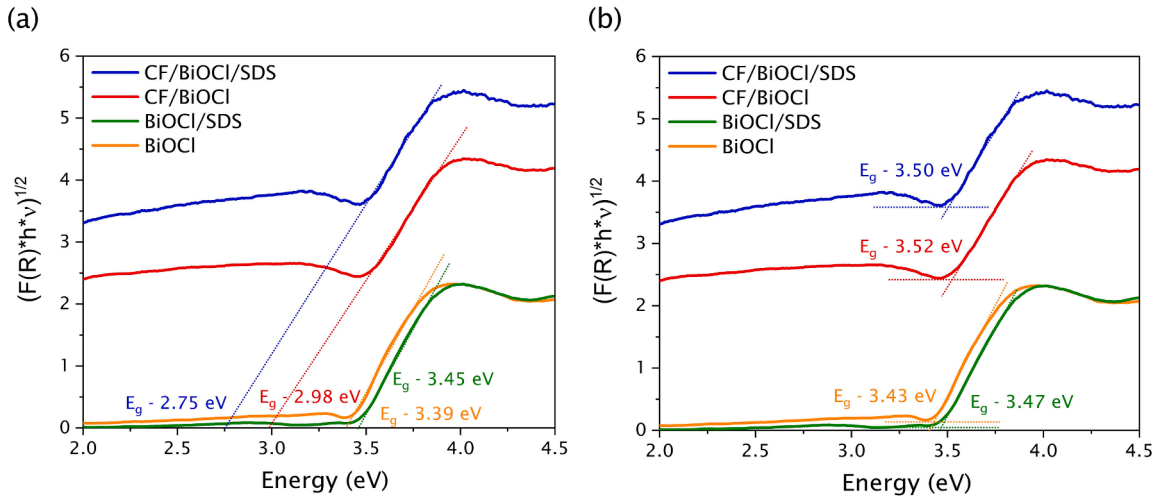

Fig. 9. Band gap calculation of the pristine BiOCl and CF-BiOCl composites from (a) zero extrapolation in Tauc representation of $(F(R)h\nu)^{1/2}$ *versus* $h\nu$, and (b) extrapolation of the linear least square fit of $(F(R)h\nu)^{1/2}$ *versus* $h\nu$ using the double fitting approach.

159.2 eV originating from Bi $4f_{5/2}$ and Bi $4f_{7/2}$, respectively (Fig. 5a). The position of the peaks corresponds to Bi^{3+}. A separation of Bi $4f_{5/2}$ and Bi $4f_{7/2}$ peaks by 5.3 eV relates to spin–orbit splitting [47]. Compared to the pristine BiOCl, the Bi 4f peaks for composites shifted to lower binding energy due to the lower valence state of bismuth, which may suggest the Bi-C bonding [48]. These peak shifts in the composites indicate a strong interfacial interaction between BiOCl and CF [37]. The deconvoluted Cl 2p spectra (Fig. 5b) displayed peaks located at 198.0 eV and 199.5 eV, corresponding to Cl $2p_{3/2}$ and Cl $2p_{1/2}$, due to the presence of Cl^- in the samples.

The deconvoluted spectra of C 1s of the composites are shown in Fig. 6a and b. The peak at 284.8 eV is ascribed to the C═C bond of the CFs. The peaks centred at 286.3 eV and 288.5 eV are attributed to the C–O and –COO implying the presence of oxygen-containing functional groups in the CFs. Besides, a small shoulder peak located at 283.5 eV in the composites can be assigned to Bi–C bonds [48]. Further, the O 1s deconvoluted spectra of the pristine BiOCl and CF-BiOCl composites are depicted in Fig. 6c–f. The peak at 529.9 eV corresponds to the O^{2-} state of lattice oxygen, which could be ascribed to the Bi-O bond in $[Bi_2O_2]$ slabs of the layered structure of the BiOCl. The peaks centred at 531.5 eV and 532.7 eV are related to the O^{2-} state of oxygen vacancies and –OH groups/adsorbed water molecules on the samples, respectively. Another

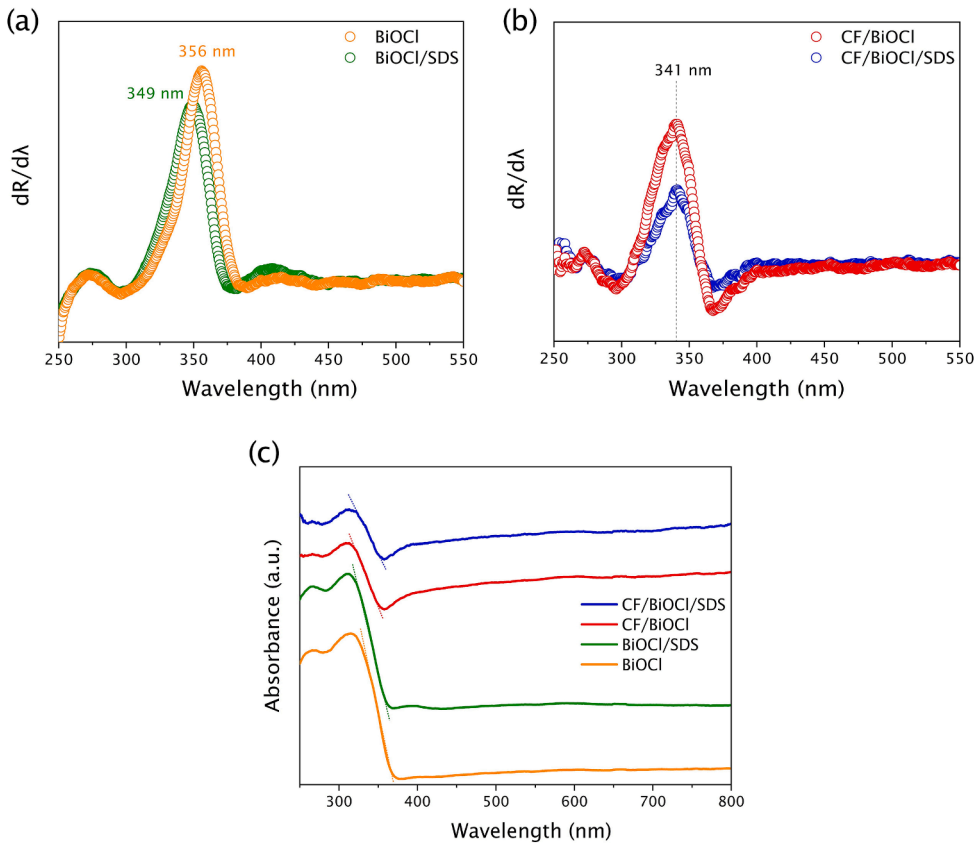

Fig. 10. First derivative DRS spectra of (a) pristine BiOCl, (b) CF-BiOCl composites, and (c) UV–Vis diffuse reflectance spectra of all samples.

peak particularly present in the composite around 534.0 eV corresponds to the O═C–O groups of the CFs [49]. To conclude, the chemical shifts of Bi 4f and Cl 2p to lower binding energies and a small intensity peak that appeared around 283.5 eV in C 1s spectra indicate a strong interfacial interaction between the CF and BiOCl.

3.2. Surface morphologies

The morphological investigation of pristine and CF-supported BiOCl with and without surfactant was done by SEM and the results are shown in Fig. 7a–h. As can be seen in Fig. 7a and b, the pristine BiOCl show more regular and thicker plates with smooth surfaces related to the tetragonal structure of BiOCl, whereas the addition of SDS forms irregular and thinner microplates (Fig. 7c and d).

In the case of composites, the hierarchical rose-like structures of BiOCl crystals were dispersed on the surface of the CFs while using the SDS, as shown in Fig. 7g, h and S2a, b. But, no such flower, rather clusters of hierarchical microplates are seen in the composites prepared without the SDS (Fig. 7e and f). Through the EDX elemental mapping of the CF-BiOCl composites (Fig. 8a and b), the distribution of Bi, O, Cl and C can be observed, revealing the formation of BiOCl on the surface of the CFs.

3.3. Optical properties

The optical properties of the samples were determined using UV–Vis diffuse reflectance spectroscopy (DRS) in the wavelength range of 200–800 nm. Due to the strong interfacial interactions between the BiOCl and CF, a mixed mechanism for the associated electronic transitions could be occurring. Most studies report that light absorption by a specific type of semiconductor and amorphous carbon proceeds through indirect allowed transition [50,51], therefore the indirect band gap energy was calculated using the Kubelka-Munk equation (Eq. (2)). The optical band gaps of the samples were primarily calculated from the zero extrapolation in the Tauc plot of $(F(R)h\nu)^{1/2}$ *versus* $h\nu$, which is about 3.39 eV and 3.45 eV for pristine BiOCl and BiOCl/SDS, respectively and a decrease in band gap (2.75 eV and 2.98 eV) was observed for the CF-BiOCl composites, as shown in Fig. 9a. However, due to the strong light absorption of carbon in the visible region, the diffuse reflectance of the composites is lower than 100% due to which the onset of the Tauc representations is no longer close to zero and appears above zero in the $(F(R)h\nu)^{1/2}$ axis. Therefore, the estimation of the band gap by the zero extrapolation of $(F(R)h\nu)^{1/2}$ is not valid which overestimates the band gap value of the composites (shown in Fig. 9a). As a result, a double linear fitting (extrapolation of the intersection of the dotted lines to zero of $(F(R)h\nu)^{1/2}$ axis) [50] was applied for the Tauc plot as shown in Fig. 9b. The estimated band gap values by the double linear approach have shown an increase in band gap values for the composites compared to the pristine BiOCl.

It is further evaluated through the first derivative DRS spectra ($dR/d\lambda$) of both reference samples and composites, which are shown in Fig. 10a and b. The absorption maximum for the pristine BiOCl samples was observed at around 349 nm (BiOCl/SDS) and 356 nm (BiOCl) (Fig. 10a). On the other hand, the CF-based composites showed a blue shift in the absorption maximum, which is around 341 nm for the composites as shown in Fig. 10b. Similar behaviour of blue shift in absorption maximum while adding carbon in the semiconductor catalyst was reported elsewhere [52,53]. This result is in line with the double linear fitting of the Tauc plot, thus the addition of carbon does not necessarily decrease the band gap and extends the absorption to the visible region.

Fig. 10c has shown that the adsorption edge of the composites seems to exhibit a red shift in the spectra between 440 and 490 nm, which could be misleading. As discussed before, the extrapolation of the linear region of the curves to zero of the y-axis provides a false interpretation. Therefore, the absorption edge can be depicted from the $dR/d\lambda$ curve

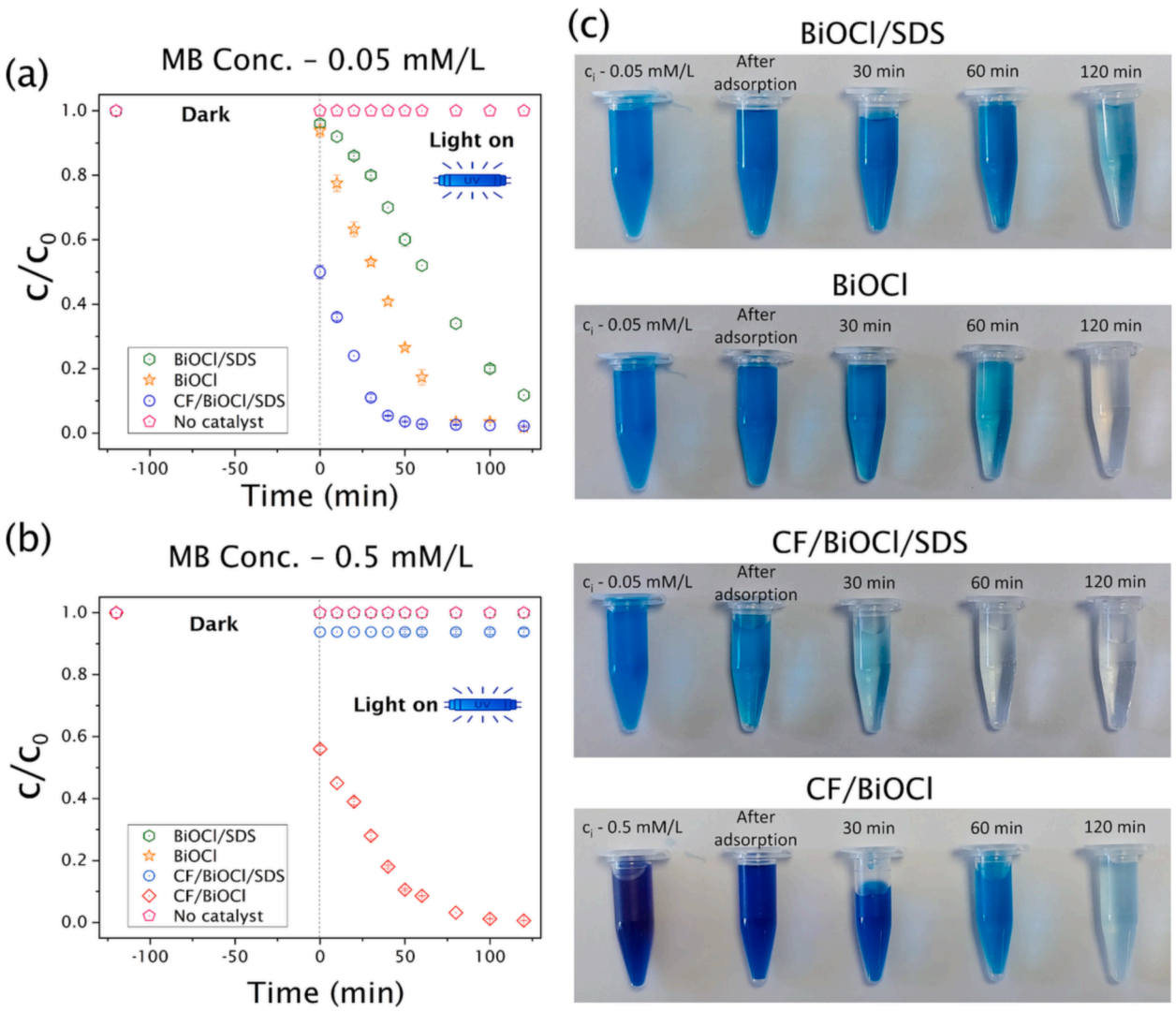

Fig. 11. Photocatalytic degradations of MB using different catalysts at (a) 0.05 mmol/L, (b) 0.5 mmol/L, and (c) photographs of MB removal test. The photolysis of MB without a catalyst is shown by pink scatter plots.

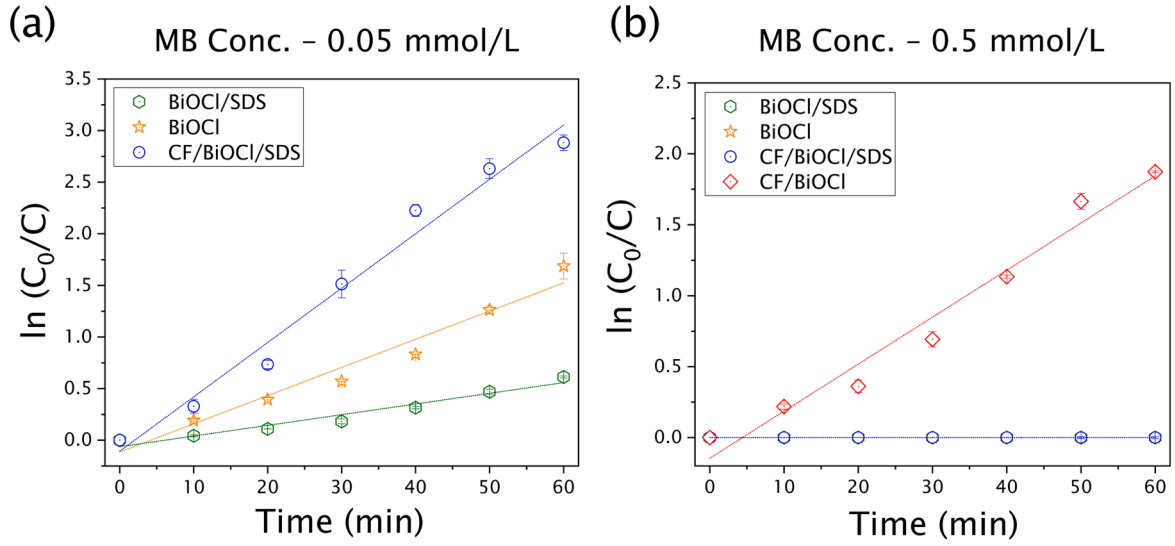

Fig. 12. The quasi-first order kinetics of the degradations of MB at different concentrations using the catalysts – (a) 0.05 mmol/L, and (b) 0.5 mmol/L.

Table 2
Rate constant values of the MB photodegradation.

Sample	MB concentration (mmol/L)	The rate constant, k (min^{-1})	R^2
BiOCl	0.05	0.0273	0.9623
BiOCl/SDS		0.0104	0.9558
CF/BiOCl/SDS		0.0522	0.9786
BiOCl	0.5	0	–
BiOCl/SDS		0	–
CF/BiOCl		0.0332	0.9695
CF/BiOCl/SDS		0	–

Table 3
Comparison of the degradation of MB by various photocatalysts under UV irradiation.

Catalyst	Concentration of MB (mg/L)	Catalyst dose (g)	Time (min)	The degradation rate of MB (%)	Ref.
BiOCl-NPls-AC	10	0.025	60	98.8	[61]
TiO_2/AC	16	0.02	90	98.2	[62]
Fe_3O_4/AC/TiO_2	100	0.1	60	98.0	[63]
Graphene-BiOCl/Fe_3O_4	–	0.01	110	80.5	[64]
ZnO-NR/ACF	50	0.01	120	99.0	[65]
Luminescent carbon material	2.2	0.015	140	99.7	[66]
TiO_2/BC	50	0.7	60	99.5	[67]
CF/TiO_2/BiOI	10	0.1	80	99.2	[68]
CF/BiOCl/SDS	16	0.2	60	97.2	This work
CF/BiOCl	160	0.2	100	99.0	This work

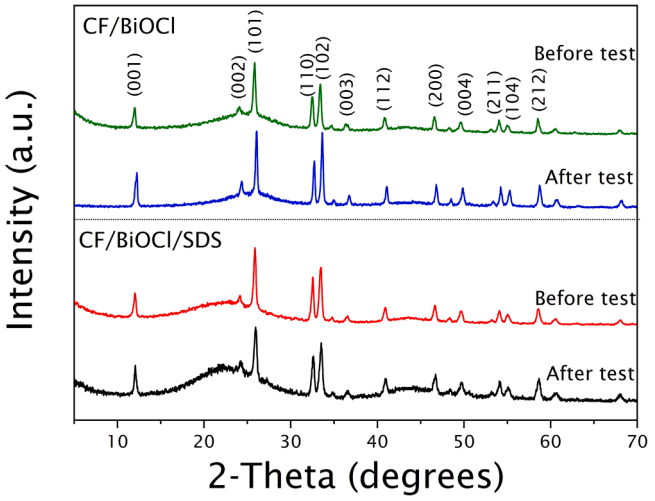

Fig. 13. The XRD diffractograms of the composites before and after the photocatalytic tests.

(Fig. 10a and b) between 380 and 388 nm for the pristine BiOCl samples and around 368 nm for the composites. Through these interpretations, we can conclude that the presence of carbon doesn't shift the absorption to the visible region for the UV-active photocatalysts like BiOCl unlike most reported. This blue shift observed in the case of composites could be due to the quantum size effect, which has been well reported in [54,55]. Also, in our case, the size reduction of the BiOCl in the composites was seen and these are the samples which showed blue shift. Therefore, we can assume the influence of lower crystallite size on the absorption edge of BiOCl.

3.4. Evaluation of photocatalytic activity

The photocatalytic activity of the catalysts was evaluated by the degradation of the MB as the model pollutant under UV-A irradiation. The degradation efficiencies of MB in the presence of different catalysts are shown in Fig. 11a and b at two different initial MB concentrations.

First, all the catalysts except CF/BiOCl were analysed with 0.05 mmol/L of MB (Fig. 11a). Since CF/BiOCl possess a relatively higher specific surface area, the photodegradation of the catalyst was analysed with a higher pollutant concentration (0.5 mmol/L), which is shown in Fig. 11b. In both concentrations, the photolysis of MB without the addition of catalyst was also tested, which is shown by pink scatter plots. At 0.05 mmol/L, the pristine BiOCl exhibited the photodegradation of MB in the following order: BiOCl (82.6%) > BiOCl/SDS (48.0%) in 60 min of irradiation. Here, the (0 0 1) facet-exposed BiOCl showed less activity than the other pristine BiOCl samples with (1 0 2) crystal orientation, as shown in Fig. 11a and S3a. At the same condition, the composite CF/BiOCl/SDS showed almost complete removal of MB (97.2%) due to its enhanced surface area, crystal orientation and hierarchical structure of BiOCl. Moreover, due to the high S_{BET} of CF/BiOCl (258.5 m^2/g), the catalyst completely removed the MB in the adsorption stage itself (in 30 min). However, at a higher MB concentration of 0.5 mmol/L, both the pristine catalysts and the CF/BiOCl/SDS exhibited no activity, since more dye molecules present in the solution absorbed the UV light and hindered the light penetration towards the surface of the catalysts. However, the composite CF/BiOCl displayed an overall removal efficiency of 99.0% in 100 min of irradiation at that high MB concentration. It has removed 44.0% of MB by adsorption due to its high specific surface area, therefore the reduced dye molecules in the solution favoured the light-harvesting efficiency of the catalyst. The higher precursor concentrations (4 mmol) have shown some changes in the formation and morphology of BiOCl crystals on the CFs, for instance, the formation of flower-like BiOCl with more hierarchical plates on CFs in the presence of SDS, but poor BiOCl crystal growth without the addition of SDS. However, there wasn't any significant influence on the structural and optical properties and also their photocatalytic performances, which are discussed in the supplementary material.

Fig. 12a and b show that the photocatalytic decolourization of MB was fitted to the Langmuir-Hinshelwood model by plotting $\ln(c_0/c)$ *versus* irradiation time (t). The pseudo-first-order kinetics was used to calculate the rate constant, k (min^{-1}) and the values at two different concentrations are given in Table 2. At 0.05 mmol/L, the rate constant of CF/BiOCl/SDS is 0.0522 min^{-1}, which is higher than that of pristine BiOCl. Moreover, the rate constant of CF/BiOCl is 0.0332 min^{-1}, which is zero for the remaining samples at high MB concentration.

Upon UV irradiation on the synthesized material, the photogenerated electrons are excited to the conduction band, which created holes (h^+) in the valence band. Electrons would be transferred to the CF at the heterojunction interface, which would enable the efficient separation of e^--h^+. The adsorption of MB on the catalyst is favourable for the transfer of charge carriers between the dye and the catalyst surface. It has been reported that e^- reduces O_2 to superoxide anion (O_2^-) while hole either oxidizes H_2O to form OH radicals or directly oxidizes MB dye. The reactive species (O_2^-, h^+, $^{\bullet}OH$) [56,57] initiate the redox reactions and degrade MB into smaller molecules like CO_2, H_2O or inorganic ions. Therefore, the color change of MB to colorless is due to the degradation of its aromatic rings.

Based on the comprehensive review by Khan et al. [58], usually, $^{\bullet}OH$ and superoxide anions (O_2^-) have been widely reported and known for the ring opening and complete degradation of methylene blue. According to a study by A. Houas *et al.* [59], the initial step in the

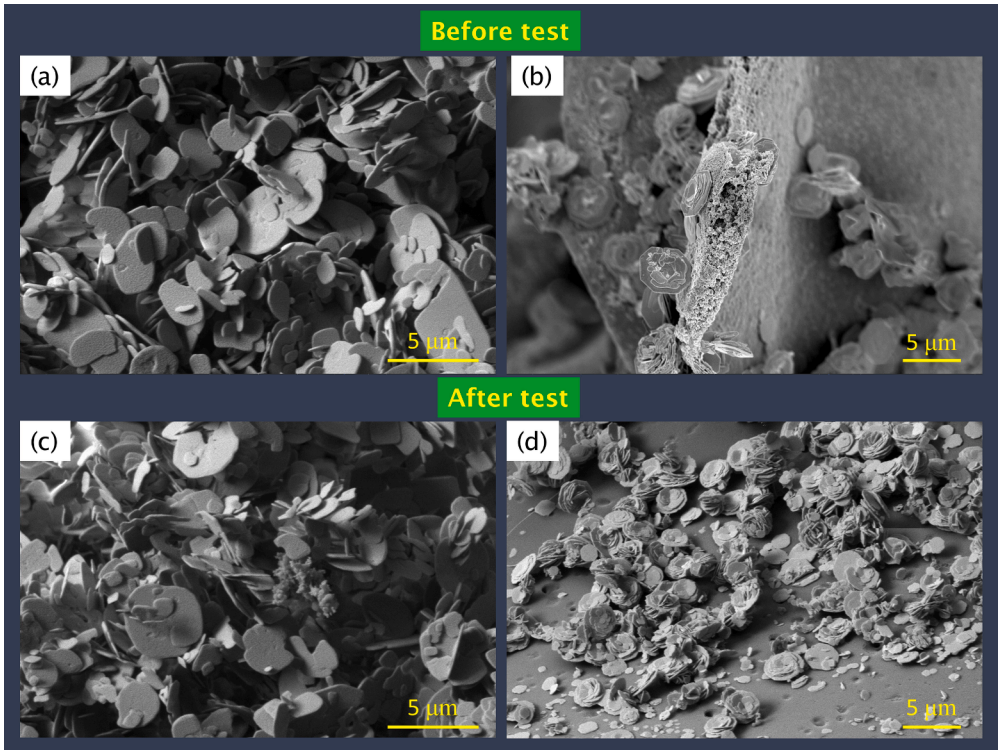

Fig. 14. SEM images of composites before and after the photocatalytic tests (a & c) CF/BiOCl, and (b & d) CF/BiOCl/SDS.

degradation of methylene blue is the attack on the C-S+=C by ˙OH followed by central aromatic ring opening containing heteroatoms, S and N, to conserve the double bond conjugation which was lost during the transformation stage of C–S+=C to C–S(=O)–C. The holes play an important role in the formation of CH and NH bonds. And the study by Wiedmer *et al.* [60] showed the degradation of MB was dependent on the generation of O_2^-/OOH. According to the above discussion, a possible degradation mechanism of MB has been proposed in steps: (a) demethylation (b) ring opening (breaking of the central aromatic ring in MB followed by side aromatic rings), (c) conversion of fragments resulting from the previous steps to the intermediate species, like phenol, R-NH_3^+, aniline and aldehydic/carboxylic species, and (d) conversion of intermediate species to simple molecules (CO_2, H_2O and NH_4^+).

Generally, in the case of porous carbon support, the rate of photodegradation is accelerated by the enhanced mass transfer and detention of the intended pollutant molecule in the pores. Thus, the hierarchical structure of CFs with high S_{BET} enables the catalyst to have more contact area for the dye molecules to promote the photocatalytic reaction and the heterojunction formed between CF and BiOCl facilitates the separation of e^- and h^+. The electrons can be transferred from BiOCl to the conductive CF through the well-connected heterojunction interfaces. Though blue shifts were seen for the composite samples, the smaller crystallite size and the higher S_{BET} of the composites facilitated the complete removal of MB. Therefore, for CF-BiOCl composites, the dominance of structural and surface area together with hierarchical morphology has contributed to the photodegradation of MB rather than the optical property.

The degradation percentage of MB by various photocatalysts under UV irradiation is summarised in Table 3. The degradation of MB by CF-supported BiOCl is comparable to, or greater than various photocatalysts reported earlier. Finally, stability tests were carried out to study the structural and morphological changes during the photocatalytic reaction. The used catalysts were washed after three cycles with ethanol and water and dried for XRD analysis. The XRD diffractogram of the composites before and after the photocatalytic tests is shown in Fig. 13.

The unchanged XRD diffraction pattern of the composite catalyst after three cycles represents their structural stability during the photocatalytic reaction. No new peaks were formed, which indicates that the crystal structure did not change significantly after the tests. The morphology of the composites was analysed using SEM (shown in Fig. 14) and no significant change in the morphology was observed before and after the tests. Therefore, the CF-supported BiOCl composites proved to be stable as a photocatalyst for MB degradation.

4. Conclusion

In this work, we proposed the applicability of waste PU elastomer-derived porous CF as a support material to the semiconductor BiOCl to improve its photocatalytic performance and overall pollutant removal efficiency. The CF-BiOCl composites were synthesized *via* the simple hydrothermal method in which the BiOCl hierarchical micro flowers and plates were immobilized on the CF surface. The determination of the band gap from diffuse reflectance through double linear fit exhibit an increased band gap of the composites, which indicates that the addition of carbon does not necessarily decrease the band gap and shifts the absorption to the visible region for the UV-active BiOCl. The photocatalytic activity of the samples was evaluated by studying the degradation of methylene blue (MB) under UV-A irradiation. Even at a high MB concentration (0.5 mmol/L), excellent photocatalytic activity was observed with an overall removal efficiency of 99.0% in 100 min of irradiation. Though a blue shift was seen for the composites in DRS, the smaller crystallite size and higher specific surface area of the composites facilitated the complete removal of MB. It is found that the dominance of structural and surface properties together with hierarchical morphology has contributed to the photodegradation of MB rather than the optical property.

Funding

This research was funded by the LIFE Programme of the European Union, LIFE19CCAHU001320. The research reported in this paper has been partly supported by the NRDI Fund TKP2021 BME-NVA based on

the charter of bolster issued by the NRDI Office under the auspices of the Ministry for Innovation and Technology.

CRediT authorship contribution statement

Mahitha Udayakumar: Visualization, Validation, Methodology, Conceptualization, Investigation, Writing – original draft. **Nikita Sharma:** Visualization, Validation, Writing – review & editing. **Klara Hernadi:** Visualization, Validation, Formal analysis, Writing – review & editing. **Matjaž Finšgar:** Validation, Resources, Investigation. **Blaz Likozar:** Resources, Investigation. **Kocserha István:** Visualization, Resources, Investigation. **Máté Leskó:** Visualization, Resources, Investigation. **Dániel Attila Karajz:** Investigation, Resources. **Imre Miklós Szilágyi:** Investigation, Resources. **Zoltán Németh:** Supervision, Project administration, Funding acquisition, Writing – review & editing.

Declaration of Competing Interest

The authors declare that they have no known competing financial interests or personal relationships that could have appeared to influence the work reported in this paper.

Data availability

No data was used for the research described in the article.

Acknowledgements

Special thanks to Dr. Mateusz Schabikowski, Institute of Nuclear Physics, Polish Academy of Sciences, for carrying out the Raman measurement. Zoltán Németh would like to thank the Hungarian Academy of Sciences Bolyai János Research Scholarship Program.

Appendix A. Supplementary data

Supplementary data to this article can be found online at https://doi.org/10.1016/j.jphotochem.2023.114812.

References

[1] A. Lebedev, F. Anariba, X.u. Li, D. Seng Hwee Leng, P. Wu, Rational design of visible-light-driven Pd-loaded α/β-Bi_2O_3 nanorods with exceptional cationic and anionic dye degradation properties, Sol. Energy 190 (2019) 531–542, https://doi.org/10.1016/j.solener.2019.08.015.

[2] B. Lin, G. Yang, L. Wang, Stacking-layer-number dependence of water adsorption in 3D ordered close-packed g-C_3N_4 nanosphere arrays for photocatalytic hydrogen evolution, Angew. Chem. 58 (2019) 4587–4591, https://doi.org/10.1002/anie.201814360.

[3] Z. Zhu, X. Tang, S. Kang, P. Huo, M. Song, W. Shi, Z. Lu, Y. Yan, Constructing of the magnetic photocatalytic nanoreactor MS@FCN for cascade catalytic degrading of tetracycline, J. Phys. Chem. C 120 (2016) 27250–27258, https://doi.org/10.1021/acs.jpcc.6b05642.

[4] F. Pincella, K. Isozaki, K. Miki, A visible light-driven plasmonic photocatalyst, Light Sci. Appl. 3 (2014) e133, https://doi.org/10.1038/lsa.2014.14.

[5] H. Wang, Y. Liang, L. Liu, J. Hu, P. Wu, W. Cui, Enriched photoelectrocatalytic degradation and photoelectric performance of BiOI photoelectrode by coupling rGO, Appl. Catal. B Environ. 208 (2017) 22–34, https://doi.org/10.1016/j.apcatb.2017.02.055.

[6] N. Sharma, Z. Pap, S. Garg, K. Hernadi, Photocatalyst Composites from Bi-based and Carbon Materials for Visible Light Photodegradation, in: S. Garg, A. Chandra (Eds.), Green Photocatalytic Semiconductors, Green Chemistry and Sustainable Technology, Springer, Cham, 2022, pp. 145–178, https://doi.org/10.1007/978-3-030-77371-7_6.

[7] M. Yadav, S. Garg, A. Chandra, R. Gläser, K. Hernadi, Green BiOI impregnated 2-dimensional cylindrical carbon block: A promising solution for environmental remediation and easy recovery of the photocatalyst, Sep. Purif. Technol. 240 (2020), 116628, https://doi.org/10.1016/j.seppur.2020.116628.

[8] Q. Zhao, X. Liu, Y. Xing, Z. Liu, C. Du, Synthesizing Bi_2O_3/BiOCl heterojunctions by partial conversion of BiOCl, J. Mater. Sci. 52 (2017) 2117–2130, https://doi.org/10.1007/s10853-016-0499-y.

[9] J. Lu, W. Zhou, X. Zhang, G. Xiang, Electronic structures and lattice dynamics of layered BiOCl single crystals, J. Phys. Chem. Lett. 11 (2020) 1038–1044, https://doi.org/10.1021/acs.jpclett.9b03575.

[10] J. Liu, L. Chen, S. Zhang, H. Zhao, Visible-light photoactive BiOCl nanosheets prepared by a solution chemistry method, Mater. Lett. 233 (2018) 174–176, https://doi.org/10.1016/j.matlet.2018.08.156.

[11] Z. Yang, Z. Shang, F. Liu, Y. Chen, X. Wang, B. Zhang, G. Liu, Hollow porous BiOCl microspheres assembled with single layer of nanocrystals: spray solution combustion synthesis and the enhanced photocatalytic properties, Nanotechnology 32 (20) (2021) 205602, https://doi.org/10.1088/1361-6528/abe575.

[12] J. Sun, Y. Cai, H. Xu, Z. Zou, M. Hu, X. Jin, L. Sun, D. Li, D. Xia, Synthesis of porous BiOCl nanocubes with enhanced visible light photocatalytic performance, Chem. Phys. Lett. 711 (2018) 207–212, https://doi.org/10.1016/J.cplett.2018.09.042.

[13] H. Li, J. Li, Z. Ai, F. Jia, L. Zhang, Oxygen vacancy-mediated photocatalysis of BiOCl: reactivity, selectivity, and perspectives, Angew. Chemie Int. Ed. 57 (2018) 122–138, https://doi.org/10.1002/anie.201705628.

[14] L. Ye, Y. Su, X. Jin, H. Xie, C. Zhang, Recent advances in BiOX (X = Cl, Br and I) photocatalysts: synthesis, modification, facet effects and mechanisms, Environ. Sci Nano. 1 (2014) 90–112, https://doi.org/10.1039/c3en00098b.

[15] H. Li, L. Zhang, Photocatalytic performance of different exposed crystal facets of BiOCl, Curr. Opin. Green Sustain. Chem. 6 (2017) 48–56, https://doi.org/10.1016/J.cogsc.2017.05.005.

[16] J. Jiang, L. Zhang, H. Li, W. He, J.J. Yin, Self-doping and surface plasmon modification induced visible light photocatalysis of BiOCl, Nanoscale 5 (2013) 10573–10581, https://doi.org/10.1039/c3nr03597b.

[17] Z. He, Y. Shi, C. Gao, L. Wen, J. Chen, S. Song, BiOCl/$BiVO_4$ p-n heterojunction with enhanced photocatalytic activity under visible-light irradiation, J. Phys. Chem. C 118 (2014) 389–398, https://doi.org/10.1021/jp409598s.

[18] A.K. Chakraborty, S.B. Rawal, S.Y. Han, S.Y. Chai, W.I. Lee, Enhancement of visible-light photocatalytic efficiency of BiOCl/Bi_2O_3 by surface modification with WO_3, Appl. Catal. A Gen. 407 (2011) 217–223, https://doi.org/10.1016/j.apcata.2011.08.040.

[19] J. Hou, Q. Dou, T. Jiang, J. Yin, J. Liu, Y. Li, G. Zhang, X. Wang, BiOCl/cattail carbon composites with hierarchical structure for enhanced photocatalytic activity, Sol. Energy 211 (2020) 1263–1269, https://doi.org/10.1016/j.solener.2020.10.051.

[20] H. Wang, L. Zhang, Z. Chen, J. Hu, S. Li, Z. Wang, J. Liu, X. Wang, Semiconductor heterojunction photocatalysts: design, construction, and photocatalytic performances, Chem. Soc. Rev. 43 (2014) 5234–5244, https://doi.org/10.1039/c4cs00126e.

[21] J. Xie, N. Guo, A. Liu, Y. Cao, J. Hu, D. Jia, Simple solid-state synthesis of BiOCl/$Bi_2O_2CO_3$ heterojunction and its excellent photocatalytic degradation of RhB, J. Alloys Compd. 784 (2019) 377–385, https://doi.org/10.1016/j.jallcom.2018.12.386.

[22] M. Guo, Z. Zhou, S. Yan, P. Zhou, F. Miao, S. Liang, J. Wang, X. Cui, Bi_2WO_6–BiOCl heterostructure with enhanced photocatalytic activity for efficient degradation of oxytetracycline, Sci. Rep. 10 (2020) 1–13, https://doi.org/10.1038/s41598-020-75003-x.

[23] J. Hou, K. Jiang, M. Shen, R. Wei, X. Wu, F. Idrees, C. Cao, Micro and nano hierachical structures of BiOI/activated carbon for efficient visible-light-photocatalytic reactions, Sci. Rep. 7 (2017) 1–10, https://doi.org/10.1038/s41598-017-12266-x.

[24] N. Sharma, Z. Pap, B. Kornélia, T. Gyulavari, G. Karacs, Z. Nemeth, S. Garg, K. Hernadi, Effective removal of phenol by activated charcoal/BiOCl composite under UV light irradiation, J. Mol. Struct. 1254 (2022), 132344, https://doi.org/10.1016/j.molstruc.2022.132344.

[25] Y. Yan, C. Ma, H. Huang, K. Yu, Y. Liu, C. Li, Z. Zhu, P. Huo, X. Tang, Y. Liu, Z. Lu, A 2D mesoporous photocatalyst constructed by the modification of biochar on BiOCl ultrathin nanosheets for enhancing the TC-HCl degradation activity, New J. Chem. 44 (2019) 79–86, https://doi.org/10.1039/c9nj05219d.

[26] S. Vadivel, J. Theerthagiri, J. Madhavan, T. Santhoshini Priya, N. Balasubramanian, Enhanced photocatalytic activity of degradation of azo, phenolic and triphenyl methane dyes using novel octagon shaped BiOCl discs/MWCNT composite, J. Water Process Eng. 10 (2016) 165–171, https://doi.org/10.1016/j.jwpe.2015.12.001.

[27] S. Yin, J. Di, M. Li, W. Fan, J. Xia, H. Xu, Y. Sun, H. Li, Synthesis of multiwalled carbon nanotube modified BiOCl microspheres with enhanced visible-light response photoactivity, CLEAN – Soil, Air Water. 44 (2016) 781–787, https://doi.org/10.1002/clen.201500418.

[28] Z. Jiang, B. Huang, Z. Lou, Z. Wang, X. Meng, Y. Liu, X. Qin, X. Zhang, Y. Dai, Immobilization of BiOX (X = Cl, Br) on activated carbon fibers as recycled photocatalysts, Dalt. Trans. 43 (2014) 8170–8173, https://doi.org/10.1039/c4dt00483c.

[29] H. Tang, T. Ju, Y. Dai, M. Wang, M. Wang, Y. Ma, G. Zheng, Synthesis and photocatalytic performance of BiOCl/graphene composite with tight interfacial contact and highly exposed (001) facets, Appl. Organomet. Chem. 36 (2022) e6526, https://doi.org/10.1002/aoc.6526.

[30] M. Inagaki, J. Qiu, Q. Guo, Carbon foam: preparation and application, Carbon N. Y. 87 (2015) 128–152, https://doi.org/10.1016/j.carbon.2015.02.021.

[31] G. Eshaq, A.E. ElMetwally, Bmim[OAc]-Cu_2O/g-C_3N_4 as a multi-function catalyst for sonophotocatalytic degradation of methylene blue, Ultrason. Sonochem. 53 (2019) 99–109, https://doi.org/10.1016/j.ultsonch.2018.12.037.

[32] Z. Derakhshan, M.A. Baghapour, M. Ranjbar, M. Faramarzian, Adsorption of methylene blue dye from aqueous solutions by modified pumice stone: kinetics and equilibrium studies, Heal. Scope 2 (2013) 136–144, https://doi.org/10.17795/jhealthscope-12492.

[33] M. Rafatullah, O. Sulaiman, R. Hashim, A. Ahmad, Adsorption of methylene blue on low-cost adsorbents: A review, J. Hazard. Mater. 177 (2010) 70–80, https://doi.org/10.1016/j.jhazmat.2009.12.047.

[34] M. Udayakumar, B. El Mrabate, T. Koós, K. Szemmelveisz, F. Kristály, M. Leskó, Á. Filep, R. Géber, M. Schabikowski, P. Baumli, J. Lakatos, P. Tóth, Z. Németh, Synthesis of activated carbon foams with high specific surface area using polyurethane elastomer templates for effective removal of methylene blue, Arab. J. Chem. 14 (7) (2021) 103214, https://doi.org/10.1016/j.arabjc.2021.103214.
[35] C. Wang, Z.-H. Shi, L. Peng, W.-M. He, B.-L. Li, K.-Z. Li, Preparation of carbon foam-loaded nano-TiO_2 photocatalyst and its degradation on methyl orange, Surfaces Interfaces 7 (2017) 116–124, https://doi.org/10.1016/j.surfin.2017.03.007.
[36] X. Qian, M. Ren, D. Yue, Y. Zhu, Y. Han, Z. Bian, Y. Zhao, Mesoporous TiO_2 films coated on carbon foam based on waste polyurethane for enhanced photocatalytic oxidation of VOCs, Appl. Catal. B Environ. 212 (2017) 1–6, https://doi.org/10.1016/j.apcatb.2017.04.059.
[37] H. Wang, X. Cai, Y. Zhang, T. Zhang, M. Chen, H. Hu, Z. Huang, J. Liang, Y. Qin, Double-template-regulated bionic mineralization for the preparation of flower-like BiOBr/carbon foam/PVP composite with enhanced stability and visible-light-driven catalytic activity, Appl. Surf. Sci. 555 (2021), 149708, https://doi.org/10.1016/j.apsusc.2021.149708.
[38] Q. Wang, J. Hui, Y. Huang, Y. Ding, Y. Cai, S. Yin, Z. Li, B. Su, The preparation of BiOCl photocatalyst and its performance of photodegradation on dyes, Mater. Sci. Semicond. Process. 17 (2014) 87–93, https://doi.org/10.1016/j.mssp.2013.08.018.
[39] D.A. Zhang, L. Chen, C. Xiao, J. Feng, L. Liao, Z. Wang, T. Wei, Facile synthesis of high 001 facets dominated BiOCl nanosheets and their selective dye-sensitized photocatalytic activity induced by visible light, J. Nanomater. 2016 (2016) 1–7, https://doi.org/10.1155/2016/5697672.
[40] L. Zhang, C.G. Niu, G.X. Xie, X.J. Wen, X.G. Zhang, G.M. Zeng, Controlled growth of BiOCl with large 010 facets for dye self-photosensitization photocatalytic fuel cells application, ACS Sustain. Chem. Eng. 5 (2017) 4619–4629, https://doi.org/10.1021/acssuschemeng.6b03150.
[41] Y.-M. Dai, W.-T. Wu, Y.-Y. Lin, H.-L. Wu, S.-H. Chen, J.-M. Jehng, J.-H. Lin, F.-Y. Liu, C.-C. Chen, Photocatalytic CO_2 reduction to CH_4 and dye degradation using bismuth oxychloride/bismuth oxyiodide/graphitic carbon nitride (BiO_mCl_n/BiO_pI_q/g-C_3N_4) nanocomposite with enhanced visible-light photocatalytic activity, Catalysts. 13 (2023) 522, https://doi.org/10.3390/catal13030522/S1.
[42] L.Z. Pei, Y. Yang, Y.Q. Pei, Synthesis of BiOCl rectangular nanostructures, E-Journal Surf. Sci. Nanotechnol. 9 (2011) 297–300, https://doi.org/10.1380/EJSSNT.2011.297.
[43] R. Jenkins, R.L. Snyder. Introduction to X-ray Powder Diffractometry, John Wiley & Sons, Inc, New York, NY, USA, 1996, https://doi.org/10.1002/9781118520994.
[44] S. Brunauer, P.H. Emmett, E. Teller, Adsorption of gases in multimolecular layers, J. Am. Chem. Soc. 60 (1938) 309–319, https://doi.org/10.1021/ja01269a023.
[45] D.A. Shirley, High-resolution X-ray photoemission spectrum of the valence bands of gold, Phys. Rev. B 5 (12) (1972) 4709–4714, https://doi.org/10.1103/PhysRevB.5.4709.
[46] S. Kang, R.C. Pawar, Y. Pyo, V. Khare, C.S. Lee, Size-controlled BiOCl–RGO composites having enhanced photodegradative properties 11 (2015) 259–275, https://doi.org/10.1080/17458080.2015.1047420.
[47] J. Rashid, S. Karim, R. Kumar, M.A. Barakat, B. Akram, N. Hussain, H. Bin Bin, M. Xu, A facile synthesis of bismuth oxychloride-graphene oxide composite for visible light photocatalysis of aqueous diclofenac sodium, Sci. Rep. 10 (2020) 1–11, https://doi.org/10.1038/s41598-020-71139-y.
[48] J. Sun, W. Tu, C. Chen, A. Plewa, H. Ye, J.A. Sam Oh, L. He, T. Wu, K. Zeng, L. Lu, Chemical bonding construction of reduced graphene oxide-anchored few-layer bismuth oxychloride for synergistically improving sodium-ion storage, Chem. Mater. 31 (2019) 7311–7319, https://doi.org/10.1021/acs.chemmater.9b01828.
[49] M. Rjeb, A. Labzour, A. Rjeb, S. Sayouri, M.C. El Idrissi, S. Massey, A. Adnot, D. Roy, C.M. Society, Contribution to the study by X-ray photoelectron spectroscopy of the natural aging of the polypropylene, moroccan J. Condens. Matter. 5 (2004) 168–172.
[50] G.D. Gesesse, A. Gomis-Berenguer, M.F. Barthe, C.O. Ania, On the analysis of diffuse reflectance measurements to estimate the optical properties of amorphous porous carbons and semiconductor/carbon catalysts, J. Photochem. Photobiol. A Chem. 398 (2020), 112622, https://doi.org/10.1016/j.jphotochem.2020.112622.
[51] J.F. Yu, T.S. Chen, H.C. Lin, S.T. Shiue, The effect of rapid thermal annealing on characteristics of carbon coatings on optical fibers, Phys. Status Solidi. 207 (2010) 379–385, https://doi.org/10.1002/pssa.200925345.
[52] N. Sharma, B. Veres, P. Dhiman, Z. Pap, K. Baán, S. Garg, K. Hernadi, Mechanistic insight of structural and optical properties of BiOCl in the presence of CNTs and investigating photodegradation of phenol by BiOCl/CNT composites, RSC Adv. 11 (2021) 37426–37435, https://doi.org/10.1039/d1ra07003g.
[53] T. Xian, H. Yang, L. Di, J. Ma, H. Zhang, J. Dai, Photocatalytic reduction synthesis of $SrTiO_3$-graphene nanocomposites and their enhanced photocatalytic activity, Nanoscale Res. Lett. 9 (2014) 1–9, https://doi.org/10.1186/1556-276X-9-327.
[54] K. Lefatshe, G.T. Mola, C.M. Muiva, Reduction of hazardous reactive oxygen species (ROS) production of ZnO through Mn inclusion for possible UV-radiation shielding application, Heliyon 6 (6) (2020), e04186, https://doi.org/10.1016/j.heliyon.2020.e04186.
[55] S. Kumar, S. Chatterjee, K.K. Chattopadhyay, A.K. Ghosh, Sol-gel-derived ZnO: Mn nanocrystals: Study of structural, Raman, and optical properties, J. Phys. Chem. C 116 (2012) 16700–16708, https://doi.org/10.1021/jp300451z.
[56] H.L. Chen, F.Y. Liu, X. Xiao, Y.Y. Lin, J. Hu, G.Y. Liu, B. Gao, D. Zou, C.C. Chen, Photoreduction of carbon dioxide and photodegradation of organic pollutants using alkali cobalt oxides $MCoO_2$ (M = Li or Na) as catalysts, J. Environ. Manage. 313 (2022), 114930, https://doi.org/10.1016/j.jenvman.2022.114930.
[57] Y.Y. Lin, K.Y. Hung, F.Y. Liu, Y.M. Dai, J.H. Lin, C.C. Chen, Photocatalysts of quaternary composite, bismuth oxyfluoride/bismuth oxyiodide/ graphitic carbon nitride: Synthesis, characterization, and photocatalytic activity, Mol. Catal. 528 (2022), 112463, https://doi.org/10.1016/j.mcat.2022.112463.
[58] I. Khan, K. Saeed, I. Zekker, B. Zhang, A.H. Hendi, A. Ahmad, S. Ahmad, N. Zada, H. Ahmad, L.A. Shah, T. Shah, I. Khan, Review on methylene blue: its properties, uses, toxicity and photodegradation, Water 14 (2022) 242, https://doi.org/10.3390/W14020242.
[59] A. Houas, H. Lachheb, M. Ksibi, E. Elaloui, C. Guillard, J.M. Herrmann, Photocatalytic degradation pathway of methylene blue in water, Appl. Catal. B Environ. 31 (2001) 145–157, https://doi.org/10.1016/S0926-3373(00)00276-9.
[60] D. Wiedmer, E. Sagstuen, K. Welch, H.J. Haugen, H. Tiainen, Oxidative power of aqueous non-irradiated TiO_2-H_2O_2 suspensions: Methylene blue degradation and the role of reactive oxygen species, Appl. Catal. B Environ. 198 (2016) 9–15, https://doi.org/10.1016/j.apcatb.2016.05.036.
[61] F. Nekouei, S. Nekouei, Comparative evaluation of BiOCl–NPls–AC composite performance for methylene blue dye removal from solution in the presence/absence of UV irradiation: Kinetic and isotherm studies, J. Alloys Compd. 701 (2017) 950–966, https://doi.org/10.1016/j.jallcom.2017.01.157.
[62] Z.A. Che Ramli, N. Asim, W.N.R.W. Isahak, Z. Emdadi, N. Ahmad-Ludin, M. A. Yarmo, K. Sopian, Photocatalytic degradation of methylene blue under UV light irradiation on prepared carbonaceous TiO_2, Sci. World J. 2014 (2014), https://doi.org/10.1155/2014/415136.
[63] S. Moosavi, R.Y.M. Li, C.W. Lai, Y. Yusof, S. Gan, O. Akbarzadeh, Z.Z. Chowhury, X. G. Yue, M.R. Johan, Methylene Blue Dye Photocatalytic Degradation over Synthesised Fe_3O_4/AC/TiO_2 Nano-Catalyst: Degradation and Reusability Studies, Nanomater 10 (2020) 2360, https://doi.org/10.3390/nano10122360.
[64] F.W.B. Zhang, Preparation of graphene-BiOCl/Fe_3O_4 nanocomposites and their use as photocatalysts for organic dyes degradation, Elastomers Compos. 52 (2017) 9–16, https://doi.org/10.7473/EC.2017.52.1.9.
[65] B. Albiss, M. Abu-Dalo, Photocatalytic degradation of methylene blue using zinc oxide nanorods grown on activated carbon fibers, Sustain 13 (2021) 4729, https://doi.org/10.3390/SU13094729.
[66] M.A. Bhatti, A. Tahira, A.A. Shah, U. Aftab, B. Vigolo, A.R. Khattab, A. Nafady, I. A. Halepoto, M. Tonezzer, Z.H. Ibupoto, Facile synthesis of a luminescent carbon material from yogurt for the efficient photocatalytic degradation of methylene blue, RSC Adv. 12 (2022) 25549–25564, https://doi.org/10.1039/d2ra04749g.
[67] B. Gong, C. Wu, H. Tian, L. Kuang, Y. Zhao, Removal of methylene blue by coupling black carbon adsorption with TiO_2 photodegradation, Toxicol. Environ. Chem. 93 (2011) 904–913, https://doi.org/10.1080/02772248.2011.566879.
[68] Y. Zhang, A. Sun, M. Xiong, D.K. Macharia, J. Liu, Z. Chen, M. Li, L. Zhang, TiO_2/BiOI p-n junction-decorated carbon fibers as weavable photocatalyst with UV–vis photoresponsive for efficiently degrading various pollutants, Chem. Eng. J. 415 (2021), 129019, https://doi.org/10.1016/j.cej.2021.129019.